



Cite this: *Phys. Chem. Chem. Phys.*,
2016, **18**, 14244

High-coverage stable structures of 3d transition metal intercalated bilayer graphene†

Ji-Hai Liao,^a Yu-Jun Zhao,^{ab} Jia-Jun Tang,^c Xiao-Bao Yang^{*ab} and Hu Xu^{*d}

Alkali-metal intercalated graphite and graphene have been intensively studied for decades, where alkali-metal atoms are found to form ordered structures at the hollow sites of hexagonal carbon rings. Using first-principles calculations, we have predicted various stable structures of high-coverage 3d transition metal (TM) intercalated bilayer graphene (BLG) stabilized by the strain. Specifically, with reference to the bulk metal, Sc and Ti can form stable TM-intercalated BLG without strain, while the stabilization of Fe, Co, and Ni intercalated BLG requires the biaxial strain of over 7%. Under the biaxial strain ranging from 0% to 10%, there are four ordered sandwich structures for Sc with the coverage of 0.25, 0.571, 0.684, and 0.75, in which the Sc atoms are all distributed homogeneously instead of locating at the hollow sites. According to the phase diagram, a homogeneous configuration of $C_8Ti_3C_8$ with the coverage of 0.75 and another inhomogeneous structure with the coverage of 0.692 were found. The electronic and magnetic properties as a function of strain were also analyzed to indicate that the strain was important for the stabilities of the high-coverage TM-intercalated BLG.

Received 18th March 2016,
Accepted 28th April 2016

DOI: 10.1039/c6cp01841f

www.rsc.org/pccp

1. Introduction

Graphene has attracted tremendous interest due to its potential applications.¹ Metal atom adsorption or doping on graphene has been extensively investigated both theoretically and experimentally, for improving and manipulating the electronic and magnetic properties of graphene to meet various requirements in device applications.^{2–8} Atomic layer deposition is an efficient surface-controlled thin-film growth technique often used to deposit metal atoms on graphene.⁹ However, due to the extended stable π orbitals of graphene and strong affinity of metal atoms toward each other, achieving uniform atomic layer deposition of metals on graphene has been experimentally difficult.¹⁰ Metal atoms generally tend to disperse inhomogeneously and cluster to form islands on the graphene sheet.^{11–14}

Alkali and alkaline earth metal adsorption and intercalation on graphite have been long studied. Ordered potassium (K) structures with coverages (x) of 1/4 and 1/3 were found on the graphite

surface, where the phase transitions between 2×2 and $\sqrt{3} \times \sqrt{3}$ were observed.¹⁵ Similar results were found for K adsorption on monolayer graphene based on the first-principles calculations, where the phase transitions between the 2×2 structure with $x = 1/4$ and the $\sqrt{3} \times \sqrt{3}$ structure with $x = 1/3$ occurred as the chemical potential of K atoms increases.¹⁶ However, there exists no stable ordered structure for Li and Ca adsorption on monolayer graphene, due to the smaller binding energy compared to the cohesive energies of the stable metal bulk phase.^{17,18} For graphite intercalation compounds (GICs), there are ordered structures LiC_6 ,^{19–21} KC_8 ,²² and CaC_6 ,²³ where CaC_6 possesses the highest superconducting transition temperature of 11.5 K. Similarly, Li, K, and Ca can also intercalate bilayer graphene (BLG) to form ordered sandwich structures C_6LiC_6 ,²⁴ C_8KC_8 ,²⁵ and C_6CaC_6 .^{26,27} In addition, the formation of triiodide and pentaiodide in the bilayer graphene has been confirmed to induce an effective hole doping, when the concentration of intercalated iodine reaches a threshold value of 6.25%.^{28,29}

Theoretically, transition metals (TMs), such as Cr ³⁰ and Mn ,^{31,32} have been reported to be suitable for doping in BLG for spintronic applications. The C_2FeC_2 and C_2CoC_2 sandwiches are all ferromagnetic metals with high spin polarization at the Fermi level, while C_2NiC_2 and C_2VC_2 sandwiches are both non-magnetic.³³ However, the phase diagram of TM-intercalated BLG is still not clear and there are several open questions: (1) are these high coverage ordered sandwich structures of C_2TMC_2 stable? (2) Are there stable ordered structures with respect to the bulk metal? (3) How can we predict the distribution patterns of 3d

^a Department of Physics, South China University of Technology, Guangzhou 510640, P. R. China. E-mail: scxyang@scut.edu.cn

^b Key Laboratory of Advanced Energy Storage Materials of Guangdong Province, P. R. China

^c Department of Chemical Engineering, Kansas State University, Manhattan, Kansas, 66502, USA

^d Department of Physics, South University of Science and Technology of China, Shenzhen, P. R. China. E-mail: xu.h@sustc.edu.cn

† Electronic supplementary information (ESI) available. See DOI: 10.1039/c6cp01841f

TM atoms adsorbed on monolayer graphene and intercalated in bilayer graphene? (4) Can we find an effective way to tailor these patterns? As reported, graphene could be experimentally stable under a strain of over 15%,^{34,35} and the adsorption energy of the Li/Ti atom on graphene increases as much as 100/71% at an applied tensile strain of 10%.³⁶ Our recent study showed that the hydrogen adsorption on Ti decorated defective graphene could be effectively modulated by the strain,³⁷ which sheds light on the stabilization of high-coverage TM-intercalated BLG.

In this paper, we have theoretically investigated various ordered structures of 3d TM-intercalated BLG with the biaxial strain. We firstly considered the primitive cell and various supercells of bilayer graphene, where the initial TM configurations were constructed according to the ordered structures of a triangular lattice. For comparison, we have also considered more intensive coverage with the corresponding supercells by nesting the hexagonal TM sheet to BLG. The results are summarized in phase diagrams as a function of biaxial strain and the chemical potential of TM. Fe, Co, and Ni prefer the C_2TMC_2 phase while Sc prefers homogenous phases. For Sc, there are four ordered phases with $x = 0.25, 0.571, 0.684, 0.75$ compared with the stable bulk metal phase. For Ti, an inhomogenous phase with $x = 0.692$ and a uniform phase with $x = 0.75$ are found. The electronic and magnetic properties were also analyzed, indicating that the strong interaction between TM atoms and graphene comes mainly from the hybridization between C-p orbitals and TM-d orbitals.

2. Methods

To investigate the structural stabilities, we define the formation energy E_γ as follows:

$$E_\gamma = E_d - E_0 - x\mu_M = E_d - E_0 - x(-E_c + \Delta\mu_M),$$

where E_d and E_0 are energies per lattice site consisting of two (four) carbon atoms for monolayer (bilayer) graphene with and without metal atoms adsorbed (intercalated), x denotes the coverage of the metal atom and $x = 1$ means that there is one metal atom in the unit cell, and μ_M is the chemical potential of metal atoms which consist of the negative cohesive energy of bulk metal $-E_c$ and $\Delta\mu_M$, where $\Delta\mu_M$ depends on the environment conditions. A tensile biaxial strain η is defined as $\eta = \Delta a/a \times 100\%$, where a is the lattice constant of free-standing graphene.

Our calculations were performed based on the density functional theory (DFT) implemented in Vienna *Ab initio* Simulation Package (VASP).³⁸ We used projector augmented wave (PAW) potentials³⁹ with generalized gradient approximation (GGA) in the Perdew–Burke–Ernzerhof (PBE)⁴⁰ format for exchange correlation potential. The plane-wave cutoff energy was set to be 450 eV and the convergence of the force on each atom to be less than 0.01 eV \AA^{-1} . The reciprocal space was represented by the Monkhorst–Pack special k point scheme⁴¹ with the density of grid points along x and y directions about $2\pi \times 0.02 \text{\AA}^{-1}$. For example, the k meshes of 12×12 and

10×10 were used for the supercells of $\sqrt{3} \times \sqrt{3}$ and 2×2 BLG, respectively, confirming that all the total energies are converged within 1 meV with the consistent energy level. A vacuum region of 15 \AA was adopted to avoid the interaction of the periodic images. Phonon spectra were investigated using PHONOPY⁴² which is based on the density functional perturbation theory (DFPT).⁴³

3. Results and discussion

Firstly, we investigated the adsorption energy of single metal atom on graphene and the interaction energy of the metal monolayer in Section 3.1, which would prejudge the stabilities of TM intercalated BLG compared to the cohesive energy of bulk metal. In Section 3.2, we constructed the initial TM configurations according to ordered structures of the triangular lattice, including the primitive cell and supercells of bilayer graphene with various coverages. Finally, we considered more intensive coverage with the corresponding supercells by nesting the hexagonal TM sheet to BLG and showed the phase diagram in Section 3.3, where the electronic and magnetic properties were also analyzed.

3.1 Single adatom adsorption on monolayer graphene

For single atom adsorption on the graphene monolayer, there are three typical adsorption sites: the hollow site (H), the top site (T), and the bridge site (B).^{44–47} We considered another X site which is at the center of the H, T, and B sites in this work (*cf.* Fig. 1(a)), and found that adatoms with the initial X site relax to the most stable adsorption site, respectively. The adsorption energy E_b is defined as $E_b = E_{\text{gra}} + E_m - E_{\text{gram}}$, where E_{gram} and E_{gra} are the total energies per supercell with and without the metal atom adsorbed, and E_m is the energy of the corresponding isolated metal atom. The adsorption energies of 3d metal atoms on 4×4 graphene are listed in Table S1 (ESI[†]). These adsorption energies are in consistent with the previous calculated values.^{2,44}

For comparison, we also take account into the TM atomic sheets and bulk structures (*cf.* Fig. 1(d) and (e)). The interaction energy E_i is defined as $E_i = E_m - E_{\text{msheet}}$, where E_{msheet} is the energy per atom of the closely packed metal sheet. The metal adsorbate on graphene would not be stable when $E_i + E_b < E_c$, *i.e.* $(E_i + E_b)/E_c < 1$, where E_c is the cohesive energy of corresponding bulk metal. As shown in Fig. 2, for the cases of Sc, Ti, Co, and Ni, $(E_i + E_b)/E_c > 1$. However, the calculated results show that the TM–graphene bilayer structure was not stable even if a biaxial strain of 10% was applied to graphene. This is due to the electrostatic repulsion of metal atoms. For metal sheet intercalated BLG, there is no stable configuration if $(E_i + E_{\text{b-BLG}})/E_c < 1$, where $E_{\text{b-BLG}}$ is the binding energy for an isolated TM atom intercalated into BLG. In the following, we focus on TM-intercalated BLG (TM = Sc, Ti, V, Fe, Co, and Ni), since they satisfy the condition of $(E_i + E_{\text{b-BLG}})/E_c > 1$. As the chemical potential of TM atoms increases, typical structures (shown in Fig. 1(f)–(h)) would be

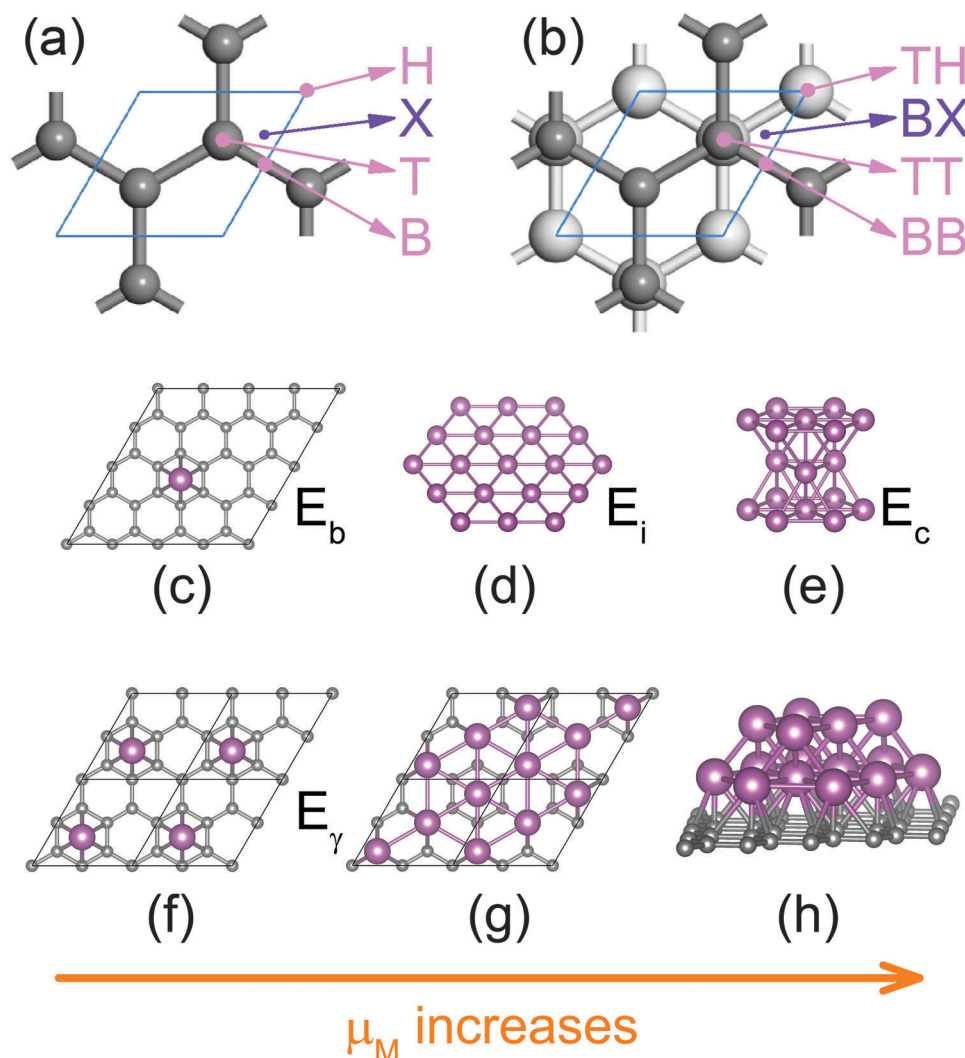


Fig. 1 (a) Atomic structure of monolayer graphene or AA stacking BLG with four adsorption or intercalated sites. H is right above the center of a carbon hexagon; T is right above a carbon atom; B is right above the middle of a C–C bond; X is the center of the H, T, and B sites. (b) Atomic structure of AB stacking BLG in which the top layer and the bottom layer are represented by small black and large grey balls and sticks. TH is right above a carbon atom of the lower graphene layer and simultaneously below the center of a carbon hexagon of the upper layer; TT is in the middle of a pair of perpendicular carbon atoms; BB is right below the middle of a C–C bond of the upper layer; BX is at the center of the TH, TT and BB sites. (c) An isolated metal atom adsorbed on monolayer graphene. (d) Metal sheet. (e) Metal bulk structure of hcp. The adsorption configurations with the coverage of (f) $x = 0.25$ and (g) $x = 0.75$ and (h) the metal cluster adsorbed on monolayer graphene as μ_M increases.

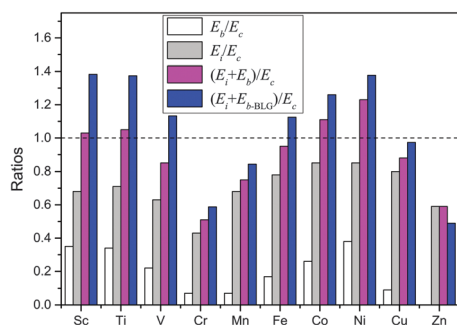


Fig. 2 The ratios of E_b/E_c , E_i/E_c , $(E_i + E_b)/E_c$, and $(E_i + E_{b-BLG})/E_c$, as a function of 3d TM elements.

found as a result of the combined actions among the TM atoms and the graphene.

3.2 TM-intercalated BLG sandwich with the biaxial strain

To consider the interlayer interaction between the two graphene layers,⁴⁸ we have adopted the dispersion correction⁴⁹ to describe the van der Waals interactions in BLG, including both AA and AB stacking. For AA stacking, the intercalated sites are similar to the adsorption sites on monolayer graphene, while for AB stacking the definitions of intercalated sites are slightly different. As shown in Fig. 1(b), the TH site is just above a carbon atom of the lower graphene layer and simultaneously below the center of a carbon hexagon of the upper layer, the TT site is in the middle of a pair of perpendicular carbon atoms, the BB site is below the middle of a C–C bond of the upper layer, and the BX site is at the center of the TH, TT, and BB sites. We constructed the initial TM-intercalated structures according to the ordered structures in the triangular lattice,^{16,50}

where the coverage x is the ratio of the number of metal atoms to that of carbon hexagonal rings with the max value of $x = 1$. The coverages of $x = 0.333$ (1/3) and $x = 0.667$ (2/3) can be achieved in the $\sqrt{3} \times \sqrt{3}$ supercell, with the coverages of $x = 0.25, 0.5, 0.75$ in the 2×2 supercell (both hexagonal and orthorhombic supercells were adopted). The distance between the two nearest atoms in the 3d TM monolayer is comparable to the graphene lattice constant of 2.46 Å (*cf.* Table S1, ESI†).

We firstly intercalate single hexagonal TM sheet between BLG with $x = 1$, where four intercalated sites were considered in both AA and AB stacking, respectively. As shown in Table S2 (ESI†), TM atoms in the AA-X site will relax to the most stable adsorption sites in AA stacking, and TM atoms in the AB-BX site will relax to the most stable adsorption sites in AB stacking. Thus, for other coverages, we only considered the initial adsorption configurations of AA-X and AB-BX sites. We also list the distances between upper graphene and lower graphene D_{G-G} in the most stable configurations, which become smaller as the strain increases.

Fig. 3 shows the phase diagrams summarizing the most stable configurations with respect to the 3d TM's chemical potential and lattice strain. For Fe-, Co-, and Ni-intercalated BLG, there exists only one ordered phase with $x = 1$, even if their chemical potential is higher than the corresponding cohesive energy. The quantum transport calculation showed a giant room-temperature magneto-resistance of 200% in the spin valve device based on the C_2FeC_2 sandwich.³³ However, we have found that the configuration of the C_2FeC_2 sandwich (*cf.* Fig. 3(a)) is metastable with reference to the corresponding cohesive energy. We have also considered the vacancy diffusion barrier with a Fe vacancy in the 4×4 supercell of the C_2FeC_2 sandwich, by using the nudged elastic-band (NEB) method.^{51,52} The calculated vacancy diffusion barrier is 0.98 eV, indicating that the configuration of the C_2FeC_2 sandwich is reasonably stable. We also investigated diffusion barriers of single 3d TM atom intercalated AB stacking BLG. The diffusion barriers for Sc, Ti, V, Cr, Mn, Fe, Co, Ni, Cu, and Zn are 0.14, 0.26, 0.23, 0.14, 0.16, 0.35, 0.25, 0.18, 0.02, and 0.00 eV, respectively. Therefore, 3d TM atoms can easily diffuse to form the TM-intercalated BLG structures.

As shown in Fig. 3(b), there exist three ordered phases for V-intercalated BLG, *i.e.* C_6VC_6 , $C_8V_2C_8$ and C_2VC_2 , with the strain larger than 7.7%. For Sc-intercalated BLG, the configuration of $C_8Sc_2C_8$ with $x = 0.5$ is only the most stable phase when strain is less than 3.5%. Under the strain ranging from 5% to 7.8%, the coverage of the most stable structures varies from 0.25 to 0.5 and 0.75 along as the Sc chemical potential changes from -1.5 eV to 0 eV, and the phase of $C_8Sc_2C_8$ vanishes with the strain larger than 7.8%. For Ti-intercalated BLG, the configuration of $C_8Ti_3C_8$ with $x = 0.75$ is only the most stable structure at the strain of less than 9.5%, and the configuration of $C_6Ti_2C_6$ with $x = 0.667$ appears under the larger strain. According to the phase diagram, the Sc/Ti clustering will not occur in the proposed graphene-TM-graphene sandwich system, while the V/Fe/Co/Ni atoms tend to form clusters in BLG, due to the smaller formation energies with

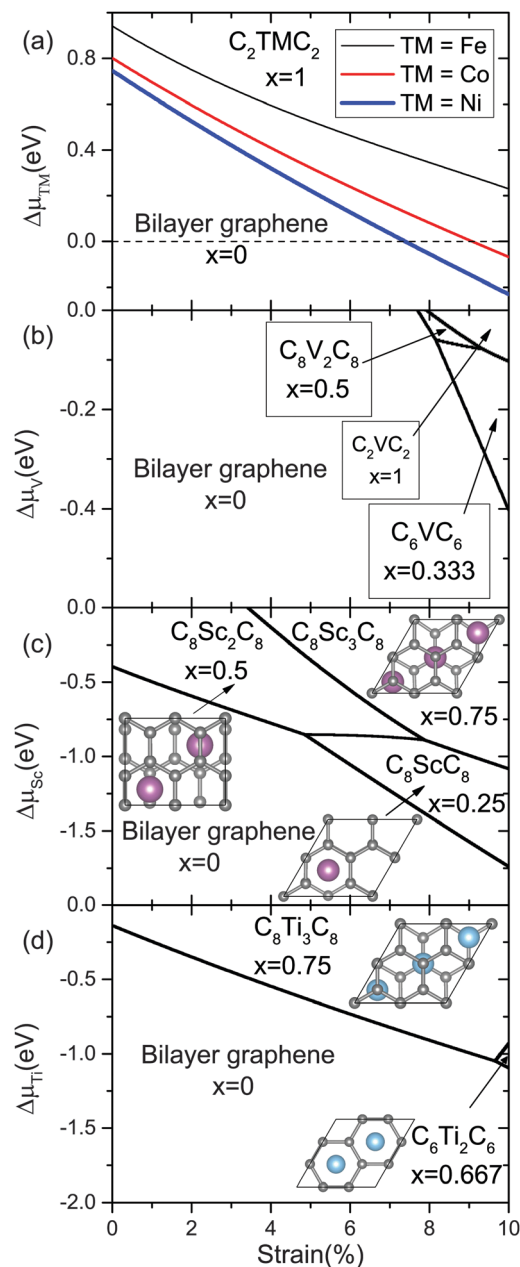


Fig. 3 The phase diagram of the most stable structures as a function of the biaxial lattice strain and the chemical potential of (a) Fe, Co, and Ni, (b) V, (c) Sc, and (d) Ti, when the TM coverages are 0, 0.25, 0.333, 0.5, 0.667, 0.75, and 1.

reference to the cohesive energies in the corresponding bulk structures.

We had also calculated the phonon spectra of $C_8Ti_3C_8$ and C_2TiC_2 under various strains, where the dynamic stability of these structures under strains is confirmed by no imaginary frequency in the spectra (see Fig. S2 and S3, ESI†). For comparison, we had calculated the phonon spectra of pure graphene without strain, which is in good agreement with the previous results.⁵³ All of the configurations of $C_2TM_xC_2$ with $x = 0.25, 0.333, 0.5, 0.667, 0.75, 1$ are stable when the biaxial tensile strain increased to 15%, but the configuration of $C_{26}Sc_4C_{26}$ with $x = 0.307$ crashes

at 15% strain. All of the configurations of $C_2TM_xC_2$ with various coverages considered in this work are found to be stable at 10% strain.

3.3 TM sheet intercalated BLG sandwich with more intensive coverage

As shown above, the configurations of $C_8Sc_3C_8$ and $C_8Ti_3C_8$ with AB stacking BLG are homogenous with one third of metal atoms at the TT site and other metal atoms at the TH site, in which there are six nearest neighbor metal atoms around each Sc or Ti atom. In the configuration of $C_8Sc_2C_8$ with a rectangular supercell, Sc atoms are located at the hollow site of a graphene and the bridge site of another graphene with translational displacement, in which the number of the nearest neighbor metal atoms around each Sc atom is four. Therefore, we might leave out possible stable phases if we only consider the initial structures from the ordered states of the triangular lattice, where TM atoms are located at the hollow sites of hexagonal carbon rings. In the following, we consider ordered phases with more intensive coverage to improve the phase diagrams.

To maintain the hexagonal symmetry, we used the $\sqrt{7} \times \sqrt{7}$, 3×3 , $2\sqrt{3} \times 2\sqrt{3}$, $\sqrt{13} \times \sqrt{13}$, $\sqrt{19} \times \sqrt{19}$, and 5×5 supercells and considered possible ordered structures with various coverages (see the ESI†). We also considered the AA and AB stacking BLG, and at least one of the TM atoms occupied the H or TH site in each initial configuration where the TM atoms are distributed uniformly. For the symmetry of a square supercell, we also reconsidered the coverages of 0.675 (81/120) and 0.720 (121/168) with a quasi-square lattice for Ti-intercalated BLG (see Fig. S5, ESI†), where there are four nearest neighbors for each TM atom.

Only the updated phase diagrams of Sc and Ti are shown in Fig. 4(a) and (b), since there is little change in the phase diagrams for V, Fe, Co, and Ni. The comparison between Fig. 3(c) and 4(a) manifests that the configurations of $C_{14}Sc_4C_{14}$ and $C_{38}Sc_{13}C_{38}$ in which Sc atoms are distributed uniformly have replaced the configuration of $C_8Sc_2C_8$. The configuration of $C_6Ti_2C_6$ is not stable compared to the configuration of $C_{26}Ti_9C_{26}$ in which Ti atoms are distributed inhomogeneously (cf. Fig. 3(d) and 4(b)).

In order to study the relative structural stability of TM intercalated BLG, we have calculated the formation enthalpy $\Delta H(x)$ as⁵⁴

$$\Delta H(x) = E_x - xE_1 - (1-x)E_0,$$

where E_x , E_1 , and E_0 are the normalized total energies with the coverage of x , 1, and 0. The formation enthalpies for Sc- and Ti-intercalated BLG as a function of coverage are shown in Fig. 4(c) and (d), respectively. The convex points indicate that the stable structure depends on the chemical potential, which is consistent with the phase diagrams. Some convex point phases did not appear in phase diagrams because the chemical potential was referred by the cohesive energy of bulk metal. For example, only $C_{14}Sc_4C_{14}$ is stable without strain in the phase diagram, while there are another two convex structures of $C_{38}Sc_{13}C_{38}$ and $C_8Sc_3C_8$. Although the experimental synthesis of such TM-intercalated BLG has not been demonstrated, Ca-intercalated BLG²⁶ was obtained from Li-intercalated BLG²⁴ by the atom-replacement method. Thus, the proposed Sc- and Ti-intercalated BLG are expected to be fabricated through the similar method, which should be further tested by the experimental studies.

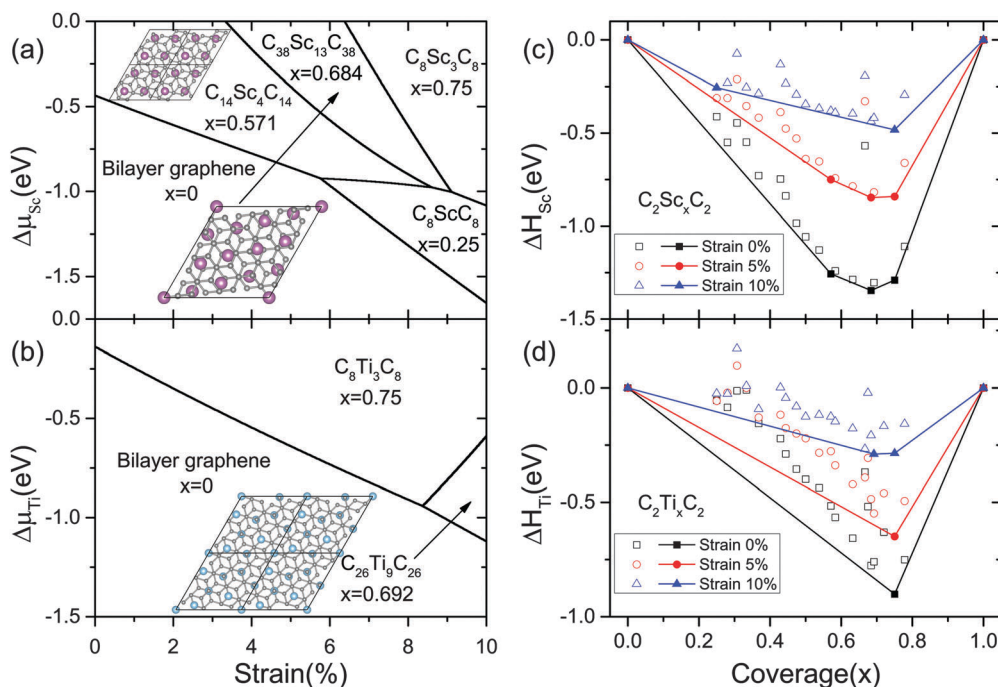


Fig. 4 Improved phase diagrams of the most stable structures as a function of the biaxial lattice strain and the chemical potential of (a) Sc and (b) Ti when considering more coverage than that of Fig. 3; and the formation enthalpy for (c) Sc- and (d) Ti-intercalated BLG as a function of coverage.

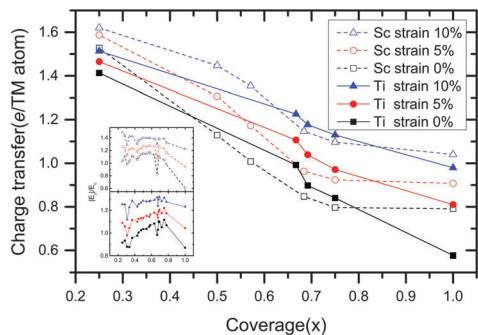


Fig. 5 The average charge transfer from the Sc or Ti atom to the outer graphenes under various strains as a function of coverage. The inset shows the ratio of the absolute value of formation energy and the cohesive energy ($|E_f|/E_c$) as a function of coverage.

The quantitative charge transfer has been calculated by the Bader charge population analysis.⁵⁵ Fig. 5 presents the average charge transfer from Sc and Ti to outer graphenes as a function of strain. Under the same strain, the charge transfer is larger for the lower coverage structures, which indicates that the covalent bond characteristic is decreased. The charge transfer also becomes larger when the strain increases for the structures with the same coverage. As shown in the inset of Fig. 5, the formation energies for $C_2Sc_xC_2$ gradually decrease with the increment of coverage, while the ones for $C_2Ti_xC_2$ have a local maximum at $x = 0.75$. Thus, there are a lot of structures close to the convex profile for $C_2Sc_xC_2$ in Fig. 4(c), indicating that these corresponding structures are relatively stable. However, few structures are close to the convex profile for $C_2Ti_xC_2$. The formation energy with the coverage of 0.75 is much larger than that of other coverages, and the phase of $C_8Ti_3C_8$ occupied most of the area of the phase diagram shown in Fig. 4(b).

Fig. 6(a) and (b) show the partial density of states (PDOS) of C-p and Sc-d orbitals of $C_{14}Sc_4C_{14}$ and $C_8Sc_3C_8$ without strain. The peak of Sc-d orbitals below the Fermi level becomes wider when the coverage increased, indicating the enhanced interaction among metal atoms. The PDOS of $C_8Sc_3C_8$ with 10% strain (*cf.* Fig. 6(c)) shows the strain induced magnetism, which is in agreement with the previous study reporting that the strain control of the magnetism generally exists for all the 3d TM atoms on graphene.⁵⁶ The strong interaction between the Sc sheet and graphenes is due to the hybridization of C-p and Sc-d orbitals which overlapped at around -1 eV, which slightly distorted the C-C network from the ideal hexagonal one. Fig. 6(d)–(f) show the PDOS of C-p and Ti-d of $C_8Ti_3C_8$ at the strain of 0%, 5%, and 10%, respectively. The peaks of Ti-d orbitals become narrower, indicating the weaker covalent bond characteristic and the enhanced ionic bond one. $C_8Ti_3C_8$ is a ferro-magnetically coupled metal (possible magnetic configurations are shown in the ESI[†]), in which one third of Ti atoms occupies the TT site and other Ti atoms reside on the TH sites. The magnetic moment comes mainly from the Ti atom at the TT site. The local magnetic moments of the TT site's Ti atom are $0.36 \mu_B$, $0.48 \mu_B$, and $0.49 \mu_B$ under the strain of 0%, 5%, and 10%, respectively. To discuss the effect of compressure, we

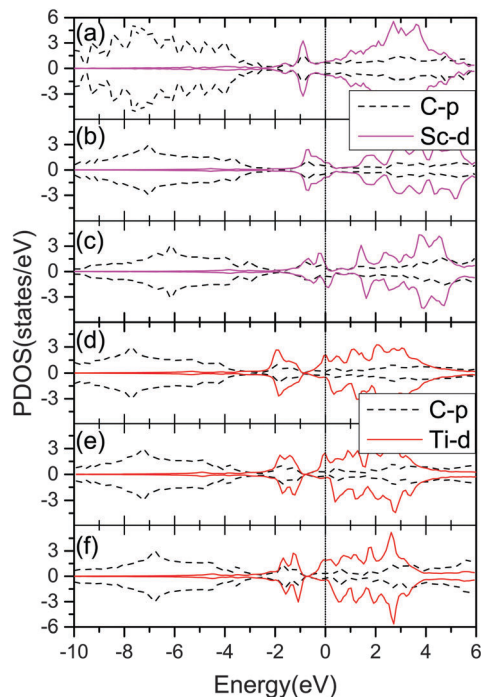


Fig. 6 The partial density of states (PDOS) for (a) $C_{14}Sc_4C_{14}$ without strain, and $C_8Sc_3C_8$ (b) without and (c) with the strain of 10%, and $C_8Ti_3C_8$ under the strain of (d) 0%, (e) 5%, and (f) 10%. The vertical dotted lines represent the Fermi level which is set to zero.

considered the cases by decreasing the D_{G-G} (D_{G-G} is the distance between bilayer graphene). As shown in Fig. S7 (ESI[†]), the magnetic moments of $C_8Ti_3C_8$ could be modulated by both the biaxial strain and the compressure of D_{G-G} . Similarly, the phase diagram could be also modified, as the compressure of D_{G-G} would destabilize the ordered states of $C_8Ti_3C_8$ (*cf.* Fig. S8, ESI[†]).

3.4 Monaxial strain on Sc- and Ti-intercalated BLG sandwiches

Since the monaxial strain may be realized more easily in experimental studies,^{57,58} we have considered the structural stability of Sc- and Ti-intercalated BLG sandwiches when the monaxial strain is applied along the armchair or zigzag direction. As shown in Fig. S9 (ESI[†]), the phase diagram of Ti-intercalated BLG with the strain along the armchair direction is almost the same as that for the zigzag direction, which indicates that the configuration of $C_8Ti_3C_8$ is the only stable phase with the monaxial strain ranging from 0% to 10%.

The phase diagrams of Sc-intercalated BLG with monaxial strain are shown in Fig. 7. The configurations of $C_{14}Sc_4C_{14}$ ($x = 0.571$) and $C_{38}Sc_{13}C_{38}$ ($x = 0.684$) appear in the phase diagram with the monaxial strain ranging from 0% to 10% along the armchair direction, while a configuration of $C_8Sc_2C_8$ ($x = 0.5$) appears when the monaxial strain is applied along the zigzag direction. In the configuration of $C_8Sc_2C_8$ (*cf.* Fig. 3(c)), the Sc atomic layer will be square as the monaxial strain of 15.5% is applied along the zigzag direction. Under the monaxial strain along the zigzag direction ranging from 0% to 10%, the Sc atomic layer of $C_8Sc_2C_8$ gradually becomes uniform, while the

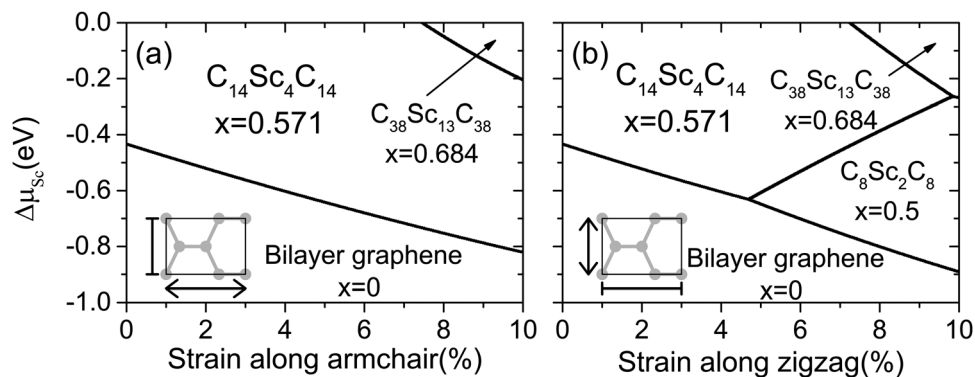


Fig. 7 The phase diagram of the most stable structures of Sc-intercalated BLG as a function of the chemical potential of Sc and the monaxial strain applied along (a) armchair and (b) zigzag directions.

one of $C_{14}Sc_4C_{14}$ tends to be distorted. According to Fig. S10 (ESI[†]), the formation enthalpy of $C_8Sc_2C_8$ could be significantly decreased as the strain along the zigzag direction increased. As a result, the structure of $C_8Sc_2C_8$ might be stabilized when the monaxial strain along the zigzag direction is greater than 4.7%.

4. Conclusions

In summary, the strain effects on the structure stability of 3d transition metals intercalated BLG were studied by the first-principles calculations. For Sc-intercalated AB stacking BLG, we obtained two interesting ordered structures. The first one is $C_{14}Sc_4C_{14}$ with the coverage of 0.571, in which a quarter of Sc atoms occupy the TH site and other Sc atoms reside on the BB site. The other one is $C_{38}Sc_{13}C_{38}$ with the coverage of 0.684, in which the Sc atoms are uniformly distributed with one thirteenth of Sc atoms occupying the TH site under the biaxial strain. A homogenous configuration of $C_8Ti_3C_8$ and another inhomogenous structure of $C_{26}Ti_9C_{26}$ were found according to the phase diagram. The configurations of $C_2Sc_xC_2$ without strain are all nonmagnetic metals, while the strain control of the magnetism exists for $C_8Sc_3C_8$. The unique ordered structure for Ti-intercalated BLG, $C_8Ti_3C_8$, is a ferromagnetic metal.

Acknowledgements

This work was supported by NSFC (Grant No. 11474100 and 11574088), Guangdong Natural Science Funds for Distinguished Young Scholars (Grant No. 2014A030306024), and the Fundamental Research Funds for the Central Universities (2015PT017). The computer times at the National Supercomputing Center in Shenzhen (NSCCSZ) and ScGrid of the Super-computing Center, Computer Network Information Center of CAS are gratefully acknowledged.

References

- 1 K. S. Novoselov, A. K. Geim, S. V. Morozov, D. Jiang, Y. Zhang, S. V. Dubonos, I. V. Grigorieva and A. A. Firsov, *Science*, 2004, **306**, 666–669.
- 2 X.-J. Liu, C.-Z. Wang, M. Hupalo, H.-Q. Lin, K.-M. Ho and M. C. Tringides, *Crystals*, 2013, **3**, 79–111.
- 3 T. Eelbo, M. Waśniowska, P. Thakur, M. Gyamfi, B. Sachs, T. O. Wehling, S. Forti, U. Starke, C. Tieg, A. I. Lichtenstein and R. Wiesendanger, *Phys. Rev. Lett.*, 2013, **110**, 136804.
- 4 K. T. Chan, J. B. Neaton and M. L. Cohen, *Phys. Rev. B: Condens. Matter Mater. Phys.*, 2008, **77**, 235430.
- 5 A. V. Krasheninnikov, P. O. Lehtinen, A. S. Foster, P. Pyykkö and R. M. Nieminen, *Phys. Rev. Lett.*, 2009, **102**, 126807.
- 6 F. Donati, Q. Dubout, G. Autès, F. Patthey, F. Calleja, P. Gambardella, O. V. Yazyev and H. Brune, *Phys. Rev. Lett.*, 2013, **111**, 236801.
- 7 F. Donati, L. Gragnaniello, A. Cavallin, F. D. Natterer, Q. Dubout, M. Pivetta, F. Patthey, J. Dreiser, C. Piamonteze, S. Rusponi and H. Brune, *Phys. Rev. Lett.*, 2014, **113**, 177201.
- 8 Y. Virgus, W. Purwanto, H. Krakauer and S. Zhang, *Phys. Rev. Lett.*, 2014, **113**, 175502.
- 9 S. M. George, *Chem. Rev.*, 2010, **110**, 111–131.
- 10 J. Zhou, Q. Sun, Q. Wang and P. Jena, *Phys. Rev. B: Condens. Matter Mater. Phys.*, 2014, **90**, 205427.
- 11 X. Liu, C. Z. Wang, Y. X. Yao, W. C. Lu, M. Hupalo, M. C. Tringides and K. M. Ho, *Phys. Rev. B: Condens. Matter Mater. Phys.*, 2011, **83**, 235411.
- 12 X. Liu, C. Z. Wang, M. Hupalo, W.-C. Lu, P. A. Thiel, K. M. Ho and M. C. Tringides, *Phys. Rev. B: Condens. Matter Mater. Phys.*, 2011, **84**, 235446.
- 13 S. M. Binz, M. Hupalo, X. Liu, C. Z. Wang, W.-C. Lu, P. A. Thiel, K. M. Ho, E. H. Conrad and M. C. Tringides, *Phys. Rev. Lett.*, 2012, **109**, 026103.
- 14 X. Liu, C.-Z. Wang, H.-Q. Lin, M. Hupalo, P. A. Thiel, K.-M. Ho and M. C. Tringides, *Phys. Rev. B: Condens. Matter Mater. Phys.*, 2014, **90**, 155444.
- 15 Z. Y. Li, K. M. Hock and R. E. Palmer, *Phys. Rev. Lett.*, 1991, **67**, 1562–1565.
- 16 X. Yang and J. Ni, *Phys. Rev. B: Condens. Matter Mater. Phys.*, 2004, **69**, 125419.
- 17 E. Lee and K. A. Persson, *Nano Lett.*, 2012, **12**, 4624–4628.
- 18 V. Wang, H. Mizuseki, H. P. He, G. Chen, S. L. Zhang and Y. Kawazoe, *Comput. Mater. Sci.*, 2012, **55**, 180–185.

- 19 J. R. Dahn, T. Zheng, Y. Liu and J. S. Xue, *Science*, 1995, **270**, 590–593.
- 20 J. M. Tarascon and M. Armand, *Nature*, 2001, **414**, 359–367.
- 21 A. S. Arico, P. Bruce, B. Scrosati, J.-M. Tarascon and W. van Schalkwijk, *Nat. Mater.*, 2005, **4**, 366–377.
- 22 N. B. Hannay, T. H. Geballe, B. T. Matthias, K. Andres, P. Schmidt and D. MacNair, *Phys. Rev. Lett.*, 1965, **14**, 225–226.
- 23 T. E. Weller, M. Ellerby, S. S. Saxena, R. P. Smith and N. T. Skipper, *Nat. Phys.*, 2005, **1**, 39–41.
- 24 K. Sugawara, K. Kanetani, T. Sato and T. Takahashi, *AIP Adv.*, 2011, **1**, 022103.
- 25 Z. Wang, S. M. Selbach and T. Grande, *RSC Adv.*, 2014, **4**, 4069–4079.
- 26 K. Kanetani, K. Sugawara, T. Sato, R. Shimizu, K. Iwaya, T. Hitosugi and T. Takahashi, *Proc. Natl. Acad. Sci. U. S. A.*, 2012, **109**, 19610–19613.
- 27 R. Shimizu, K. Sugawara, K. Kanetani, K. Iwaya, T. Sato, T. Takahashi and T. Hitosugi, *Phys. Rev. Lett.*, 2015, **114**, 146103.
- 28 H. Kim, O. Renault, A. Tyurnina, J.-P. Simonato, D. Rouchon, D. Mariolle, N. Chevalier and J. Dijon, *Appl. Phys. Lett.*, 2014, **105**, 011605.
- 29 D. Tristant, P. Puech and I. C. Gerber, *Phys. Chem. Chem. Phys.*, 2015, **17**, 30045–30051.
- 30 J. Thakur, M. K. Kashyap, H. S. Saini and A. H. Reshak, *J. Alloys Compd.*, 2015, **649**, 1300–1305.
- 31 Y. Mao and J. Zhong, *Nanotechnology*, 2008, **19**, 205708.
- 32 T. P. Kaloni, M. U. Kahaly and U. Schwingenschloegl, *J. Mater. Chem.*, 2011, **21**, 18681–18685.
- 33 J. Zhou, L. Wang, R. Qin, J. Zheng, W. N. Mei, P. A. Dowben, S. Nagase, Z. Gao and J. Lu, *J. Phys. Chem. C*, 2011, **115**, 25273–25280.
- 34 C. Lee, X. D. Wei, J. W. Kysar and J. Hone, *Science*, 2008, **321**, 385–388.
- 35 K. S. Kim, Y. Zhao, H. Jang, S. Y. Lee, J. M. Kim, K. S. Kim, J.-H. Ahn, P. Kim, J.-Y. Choi and B. H. Hong, *Nature*, 2009, **457**, 706–710.
- 36 M. Zhou, Y. Lu, C. Zhang and Y. P. Feng, *Appl. Phys. Lett.*, 2010, **97**, 103109.
- 37 J.-H. Liao, Y.-J. Zhao and X.-B. Yang, *Int. J. Hydrogen Energy*, 2015, **40**, 12063–12071.
- 38 G. Kresse and J. Furthmüller, *Comput. Mater. Sci.*, 1996, **6**, 15–50.
- 39 P. E. Blöchl, *Phys. Rev. B: Condens. Matter Mater. Phys.*, 1994, **50**, 17953–17979.
- 40 J. P. Perdew, K. Burke and M. Ernzerhof, *Phys. Rev. Lett.*, 1996, **77**, 3865–3868.
- 41 H. J. Monkhorst and J. D. Pack, *Phys. Rev. B: Solid State*, 1976, **13**, 5188–5192.
- 42 A. Togo, F. Oba and I. Tanaka, *Phys. Rev. B: Condens. Matter Mater. Phys.*, 2008, **78**, 134106.
- 43 X. Gonze and C. Lee, *Phys. Rev. B: Condens. Matter Mater. Phys.*, 1997, **55**, 10355–10368.
- 44 C. Cao, M. Wu, J. Jiang and H.-P. Cheng, *Phys. Rev. B: Condens. Matter Mater. Phys.*, 2010, **81**, 205424.
- 45 T. P. Hardcastle, C. R. Seabourne, R. Zan, R. M. D. Brydson, U. Bangert, Q. M. Ramasse, K. S. Novoselov and A. J. Scott, *Phys. Rev. B: Condens. Matter Mater. Phys.*, 2013, **87**, 195430.
- 46 H. Sevinçli, M. Topsakal, E. Durgun and S. Ciraci, *Phys. Rev. B: Condens. Matter Mater. Phys.*, 2008, **77**, 195434.
- 47 Y. Sanchez-Paisal, D. Sanchez-Portal and A. Ayuela, *Phys. Rev. B: Condens. Matter Mater. Phys.*, 2009, **80**, 045428.
- 48 I. V. Lebedeva, A. A. Knizhnik, A. M. Popov, Y. E. Lozovik and B. V. Potapkin, *Phys. Chem. Chem. Phys.*, 2011, **13**, 5687–5695.
- 49 S. Grimme, *J. Comput. Chem.*, 2006, **27**, 1787–1799.
- 50 X. Yang and J. Ni, *Phys. Rev. B: Condens. Matter Mater. Phys.*, 2003, **67**, 195403.
- 51 G. Henkelman and H. Jónsson, *J. Chem. Phys.*, 2000, **113**, 9978–9985.
- 52 G. Henkelman, B. P. Uberuaga and H. Jónsson, *J. Chem. Phys.*, 2000, **113**, 9901–9904.
- 53 F. Liu, P. Ming and J. Li, *Phys. Rev. B: Condens. Matter Mater. Phys.*, 2007, **76**, 064120.
- 54 S. V. Barabash, V. Blum, S. Müller and A. Zunger, *Phys. Rev. B: Condens. Matter Mater. Phys.*, 2006, **74**, 035108.
- 55 G. Henkelman, A. Arnaldsson and H. Jónsson, *Comput. Mater. Sci.*, 2006, **36**, 354–360.
- 56 B. Huang, J. Yu and S.-H. Wei, *Phys. Rev. B: Condens. Matter Mater. Phys.*, 2011, **84**, 075415.
- 57 Q. Liu, M. Zhang, L. Huang, Y. Li, J. Chen, C. Li and G. Shi, *ACS Nano*, 2015, **9**, 12320–12326.
- 58 C. Si, Z. Sun and F. Liu, *Nanoscale*, 2016, **8**, 3207–3217.